The Astrophysical Journal, 773:27 (11pp), 2013 August 10 doi:10.1088/0004-637X/773/1/27

UNEXPECTED IONIZATION STRUCTURE IN ETA CARINAE'S "WEIGELT KNOTS"*

Grant N. Remmen[1,2], Kris Davidson[1], and Andrea Mehner[3]
[1] School of Physics and Astronomy, University of Minnesota, Minneapolis, MN 55455, USA
[2] California Institute of Technology, Pasadena, CA 91125, USA
[3] ESO, Alonso de Cordova 3107, Santiago de Chile, Chile
Received 2013 January 31; accepted 2013 June 1; published 2013 July 22

ABSTRACT

The Weigelt knots, dense slow-moving ejecta near η Carinae, are mysterious in structure as well as in origin. Using spatially dithered spectrograms obtained with the *Hubble Space Telescope*/Space Telescope Imaging Spectrograph (*HST*/STIS), we have partially resolved the ionization zones of one knot. Contrary to simple models, higher ionization levels occur on the *outer* side, i.e., farther from the star. They cannot represent a bow shock, and no satisfying explanation is yet available—though we sketch one qualitative possibility. STIS spectrograms provide far more reliable spatial measurements of the Weigelt knots than *HST* images do, and this technique can also be applied to the knots' proper motion problem. Our spatial measurement accuracy is about 10 mas, corresponding to a projected linear scale of the order of 30 AU, which is appreciably smaller than the size of each Weigelt knot.

Key words: circumstellar matter – stars: emission-line, Be – stars: individual (eta Carinae) – stars: variables: general – stars: winds, outflows

1. THE WEIGELT KNOTS

Many years ago, speckle imaging techniques revealed compact brightness peaks within 0.″3 of η Carinae (Weigelt & Ebersberger 1986; Hofmann & Weigelt 1988). Observations with the *Hubble Space Telescope (HST)* later showed emission-line spectra there (Davidson et al. 1995, 1997; Weigelt & Kraus 2012; Hamann 2012).

Often called the "Weigelt knots" or "Weigelt blobs," these objects have extraordinary attributes: (1) they move outward from the star at much lower speeds than η Car's other ejecta, $V \sim 40$ km s^{-1} instead of $V > 300$ km s^{-1}; (2) they were ejected significantly later than the star's great eruption of 1830–1860 (Weigelt et al. 1995; Davidson et al. 1997; Dorland et al. 2004; Smith et al. 2004); and (3) they produce thousands of narrow emission lines of Fe^{+}, Fe^{++}, and other species (Zethson 2001; Zethson et al. 2012). They are rather dense by nebular standards, $n_{\rm H} > 10^7$ cm^{-3}. Doppler shifts and astrometry indicate locations 300–1000 AU from the central star, and fairly close to the equatorial plane of the bipolar Homunculus ejecta nebula. Most authors suspect an origin in the "second eruption" observed around 1890 (e.g., Weigelt et al. 1995; Davidson et al. 1997; Smith et al. 2004; Smith 2012; Weigelt & Kraus 2012); but, for reasons noted in Section 2, this surmise is difficult to prove. Indeed, since infrared images do not closely match those made at visual wavelengths (Artigau et al. 2011), the features might conceivably be illusions caused by local minima in the circumstellar extinction, rather than physical condensations. In summary, the Weigelt knots are known only in a rudimentary sense, and they have certainly not been explained.

Their emission lines are presumably excited, directly or indirectly, by radiation from the central binary star. Observed spectra appear consistent with this hypothesis (Hamann 2012), and alternatives such as shock excitation have serious energy-supply difficulties (Section 5). Therefore, the knots' spectra and ionization structure contain valuable information about the UV output of both central stars, if we can understand and quantify the morphology. In this paper, we report the first observations of spatial ionization structure in a Weigelt knot.

The Fe II, [Fe II], and other low-ionization features result from a combination of UV fluorescence plus ordinary thermal collisions in H^0/H^+, He^0 zones (Hamann 2012). The He I, [Ne III], and [Ar III] lines, however, arise in He^+ zones which require helium-ionizing photons, $h\nu > 25$ eV. Since the primary star is too cool, these are thought to be supplied by the hot secondary star (see Mehner et al. 2010, and references therein). Based on likely parameters, one expects high-ionization zones of He^+, Ne^{++}, etc., to exist in parts of the Weigelt knots that face toward the central star (Osterbrock & Ferland 2006; Davidson & Netzer 1979). In other words, the simplest model predicts an inverse correlation between ionization level and distance from the star. The size scale of the zones should help to constrain the local density values and the FUV output of the secondary star.

Here we describe spatially resolved measurements of ionization zones in Weigelt knot "C." But our main result is counter-intuitive, almost paradoxical: *the stratification appears to be inverted,* with higher ionization at larger projected distances from the central star. No satisfying explanation has yet been proposed.

2. OBSERVATIONAL DIFFICULTIES AND A METHOD BASED ON SPECTROGRAMS

Three main unsettled observational problems require spatial resolution of the Weigelt knots: their proper motions, sizes, and ionization structure. Their projected locations are 100 to 300 mas from the star, with sizes of the order of 100 mas, requiring measurement accuracies better than 20 mas. Standard *HST* imaging (see, e.g., Dorland et al. 2004; Smith et al. 2004; Weigelt & Kraus 2012, and references therein) has proven inadequate for several reasons.

1. The image of the central star seriously contaminates those of the knots. With most available filters the peak brightness of each knot is less than 4% that of the central star, and the instrumental point-spread function (PSF) has intricate

* Based on observations made with the NASA/ESA *Hubble Space Telescope.* STScI is operated by the Association of Universities for Research in Astronomy, Inc., under the NASA contract NAS 5-26555.

structure at comparable levels out to $r \sim 300$ mas.[4] An example of the small knot/star brightness ratio will be noted at the end of Section 3.3.

2. Standard processing techniques do not fully remove the central star from *HST* images. Experience shows that simple linear subtraction leaves illusory features around $r \sim 200$ mas, weak but sufficient to perturb any measurement of the Weigelt knots. Worse, the same is true for standard deconvolution procedures. The reasons are beyond the scope of this paper, but concrete examples can be seen in Figures 1–3 of Smith et al. (2004). Those authors attempted to deconvolve *HST*/ACS images of η Car, but their results show obvious remnants of a circular "ring of beads" which is part of the *HST*'s basic PSF (Krist et al. 2011, and references therein). In later Advanced Camera for Surveys (ACS) images with different *HST* roll angles, some of those spots rotated with the instrument.[5]
3. Every *HST* image of the Weigelt knots samples a mixture of continuum plus emission lines. Since the continuum largely represents dust-reflected light from the star, its spatial distribution very likely differs from that of the line-emitting gas (Hamann 2012; Artigau et al. 2011). In order to estimate the relative contributions, one must examine spectra as discussed below.

These circumstances cast serious doubt on any measurements of the knots in *HST* images; indeed, some of the published measurement sets contain statistical hints of extraneous effects. A few special near-IR images are better (see, e.g., Figure 4 in Artigau et al. 2011), but there are not enough of them to give much information about ionization structure, motions, etc.

The difficulties become far less serious if we employ *HST* slit spectrograms rather than images. Many of the Weigelt knots' emission lines have peak brightnesses far above the continuum. Moreover, we can take advantage of the narrowness of these lines ($\Delta V < 60$ km s^{-1}) to measure and remove contamination by the underlying star image. The Space Telescope Imaging Spectrograph (STIS) is well adapted to this task.

In the following, we seek to measure each Weigelt-knot emission-line's *spatial* profile, not its spectral profile or intensity. Of course, we must remove contamination by the star's PSF halo and the knot's continuum. If the star's spectrum is essentially a continuum at the wavelength of the narrow emission line being measured, then the effective contamination can be assessed at wavelengths on each side of the line. Weak features in the star's spectrum do not cause serious errors, because they are much broader than any Weigelt-knot emission line. Operationally, there is no need to distinguish between the knot's underlying continuum and the star's PSF halo; both are subtracted together. This procedure cannot be done with images, because no available imaging camera with very high spatial resolution has adequate sets of closely spaced narrowband filters. In an *HST*/STIS spectrogram, on the other hand, the underlying continuum contamination can be measured in CCD columns near the emission line (see below). Two strong advantages of our approach are: (1) the contamination is removed without any need for deconvolution and (2) the continuum samples occur in the same observation as the emission line, thereby assuring data homogeneity.

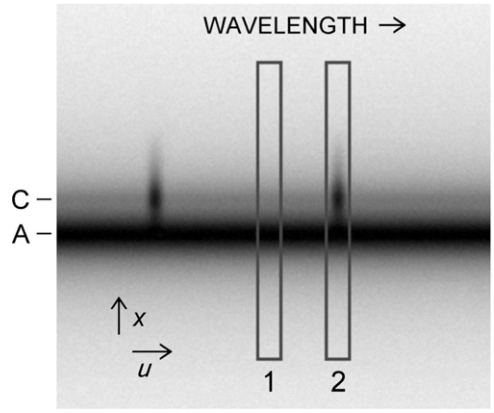

Figure 1. Narrow wavelength interval in a simulated spectrogram, showing our basic measurement procedure. "A" and "C" are the spectra of the central star and Weigelt knot C; two narrow emission lines of the latter can be seen. Various complications are noted in the text.

Apart from complications noted in Section 3, our basic approach is fairly obvious. Figure 1 shows a small wavelength interval in a fictitious, idealized slit spectrogram. Light source A is the central star and C is one of the Weigelt knots. For simplicity, the star's spectrum is depicted as a continuum. Two emission lines of C can be seen in the figure, and here we measure the net *spatial* profile of the one on the right. If x denotes position along the slit, we extract two separate samples $f(x)$: sample 1 avoids spectral features in both A and C, while sample 2 includes the chosen emission line in knot C. Each of these is a sum of adjoining CCD columns, but there is no need to include or measure the total intensity of the line. After sample 1 has been renormalized to correct for the wavelength dependence of the continuum flux, the difference $f_2(x) - f_1(x)$ represents only the emission line arising in knot C. If the spatial profile $f_1(x)$ depends on wavelength, we can parameterize it by extracting more samples.

In practice, this approach works quite well (Section 3.3). The star subtraction is simpler and more robust than one can achieve in an *HST* image, because it requires only data from a small vicinity on the same spectrogram. (In order to remove the star's optical halo from an ordinary image, either by subtraction or by deconvolution, one must derive the structure of its image based on optical modeling or another star image; and η Car's profile probably differs from a point-source PSF. The spectrogram method practically eliminates this difficulty.) A mild nonlinearity of the detector response would invalidate conventional methods of removing the central star optical halo in an image, but has only a second-order influence with our method. And, most important, for many narrow emission lines the brightness ratio C/A is far greater than in any available non-spectroscopic image.

In order to obtain adequate spatial sampling with the STIS/CCD, one must employ "dithered" observations (Section 3). Since no such data were obtained before our observations in 2010 (see below), we have not yet attempted to apply this method to the proper motion and ejection-date puzzle. Instead we focus on another, equally significant problem: the knots' ionization structure mentioned in Section 1.

We chose narrow emission lines in four physically distinct categories:

[4] The one relevant exception is narrowband filter F631N used with the Wide Field Camera (*HST*/WFPC2). In an image made with this filter, 10%–20% of the Weigelt-knot signal may represent [S III] λ6314 (Mehner et al. 2010). But most of the signal is due to other emission and/or reflection, and images give no information about the relative contributions. Moreover, the *HST* PSF is relatively broad at $\lambda > 6000$ Å.

[5] J. Ely (2010, private communication); unpublished data analyses.

Table 1
Narrow Emission Lines Measured in Weigelt Knot C

Label and Category[a]	ID[b]	λ_{vac} (Å)	Transition[b]	E_2[c] (eV)	E_1[c] (eV)
1 X	Fe II	2507.55	$c^4F_{7/2}$–$5p^6F_{9/2}$	11.167	6.222
2 X	Fe II	2509.10	$c^4F_{7/2}$–$4p^4G_{9/2}$	11.164	6.222
3 H	[Ne III] (1F)	3869.85	$2p^4\,^3P_2$–$2p^4\,^1D_2$	3.204	0
4 L	Fe II (3)	3939.41	$a^4P_{5/2}$–$z^6D_{5/2}$	4.818	1.671
5 L	[Ni II] (3F)	3994.19	$a^2D_{5/2}$–$b^2D_{5/2}$	3.104	0
6 H	He I (18)	4027.33	$2p\,^3P$–$5d\,^3D$	24.043	20.964
7 L	[S II] (1F)	4069.75	$3p^3\,^4S_3/2$–$3p^3\,^2P_3/2$	3.046	0
8 L	Fe II (38)	4585.12	$b^4F_{9/2}$–$z^4D_{7/2}$	5.511	2.807
9 L	Fe II (37)	4630.64	$b^4F_{9/2}$–$z^4F_{9/2}$	5.484	2.807
10 L	[Fe II] (4F)	4640.97	$a^6D_{3/2}$–$b^4P_{1/2}$	2.778	0.107
11 M	[Fe III] (3F)	4659.35	$3d^6\,^5D_4$–$3d^6\,^3F2_4$	2.661	0
12 M	[Fe III] (3F)	4702.85	$3d^6\,^5D_3$–$3d^6\,^3F2_3$	2.690	0.054
13 L	[Fe II] (4F)	4729.39	$a^6D_{5/2}$–$b^4P_{3/2}$	2.704	0.083
14 L	[Fe II] (20F)	4776.05	$a^4F_{9/2}$–$b^4F_{7/2}$	2.828	0.232
15 L	[Fe II] (20F)	4815.88	$a^4F_{9/2}$–$b^4F_{9/2}$	2.807	0.232
16 H	He I (10)	7067.20	$2p\,^3P$–$3s\,^3S$	22.718	20.964
17 H	[Ar III] (1F)	7137.76	$3p^4\,^3P_2$–$3p^4\,^1D_2$	1.737	0
18 L	[Fe II] (14F)	7157.13	$a^4F_{9/2}$–$a^2G_{9/2}$	1.964	0.232
19 L	[Fe II] (14F)	7173.98	$a^4F_{7/2}$–$a^2G_{7/2}$	2.030	0.301

Notes.
[a] L, M, and H: low, moderate, or high ionization; X: "exotic," see the text.
[b] Zethson (2001); Zethson et al. (2012).
[c] http://physics.nist.gov/PhysRefData/ASD/levels_form.html.

L, low ionization: Fe II, [Fe II], and other species that can occur in either an H^0 or an H^+ zone.

M, moderate ionization: [Fe III]. Since the ionization potential of Fe^+ is 16.2 eV, Fe^{++} tends to coexist with H^+ and He^0.

H, high ionization: He I, [Ar III], and [Ne III], representing He^+ zones. (The He I lines are due to recombination.) He^0, Ar^+, and Ne^+ have ionization potentials of 24.6, 27.6, and 41.0 eV, respectively, presumably requiring photons from the hot secondary star (see Mehner et al. 2010, and references therein).

X, exotic: Fe II λλ2508, 2509. Pumped by Lyα, these extraordinary features have laser-like properties almost unique in astrophysics (Johansson & Letokhov 2004; Hamann 2012; Johansson & Hamann 1993; Davidson et al. 1997).

The high-ionization lines were once suspected to come either from a diffuse region in which the Weigelt knots are imbedded, or perhaps from gas between the star and the knots (Verner et al. 2005). Mehner et al. (2010) showed, however, that [Ne III] has brightness maxima near the knots. STIS data available for that investigation could not resolve each knot, because they were not dithered to obtain good spatial sampling. If the knots are real density concentrations, then the nature of photoionization leads one to predict stratified ionization zones as noted in Section 1. The relative location of Fe II λλ2508, 2509 is potentially valuable because it is model dependent: it might occur in the moderate ionization zone because Lyα photons from the stellar wind have difficulty penetrating the low-ionization zone, and some Fe^+ ions coexist with Fe^{++} (see Hamann 2012, and references therein).

Using the *HST*/STIS observations described in Section 3, we measured the 19 emission lines listed in Table 1. Suitable data were available in four wavelength intervals, and we chose well-defined isolated lines, excluding blends and also avoiding strong features in the star's spectrum. For instance, we omitted [Ne III] λ3969 because it is confused with other strong features. [Ar III] λ7138 has too long a wavelength for *HST*'s best resolution, but it gave useful results (Section 4). Spectral traces in Figure 2 show most of the selected emission lines. The UV spectral region is not shown, because λλ2508, 2509 hugely exceeds all other features there; see Figure 8 in Davidson et al. (1997), Figure 5.5 in Hamann (2012), and Figure A.3 in Zethson et al. (2012).

3. THE DATA SET AND DETAILED METHODS

Since our procedure was carefully adapted to a non-routine purpose, it requires a lengthy explanation. Readers interested mainly in the results, and willing to trust our precautions, may choose to skip most of this section.

We obtained suitable data with the STIS/CCD on 2010 March 3 (Table 2). Apart from spatial dithering (see below), we used conventional instrument parameters. The slit width was approximately 100 mas or 2 CCD columns, a peakup was used to place the slit midline on the star, and the slit was oriented along position angle 302°, which intersects Weigelt knot C. The nominal spatial scale was 50.7 mas per CCD row, but a small error in this quantity affects only the scale factor of our relative measurements. For most of the emission lines we used STIS grating G430M, whose dispersion was about 0.3 Å per CCD column. For Fe II λλ2508, 2509 we used grating G230MB with 0.15 Å per column, and for some far-red lines the grating was G750M with 0.56 Å per column. In each case, the spectral resolution was about 2 CCD columns. The typical intrinsic line width in knot C, 20–40 km s^{-1}, amounts to less than 2 CCD columns. These data are publicly available in the *HST* archive and at the η Car Treasury Program Web site.[6] For other information see the STIS instrument handbook.[7]

The STIS/CCD has a serious deficiency: its 50.7 mas pixel size is too large to take good advantage of *HST*'s spatial resolution in any single exposure (Davidson 2006). Fortunately

[6] http://etacar.umn.edu/.
[7] http://www.stsci.edu/hst/stis/documents/.

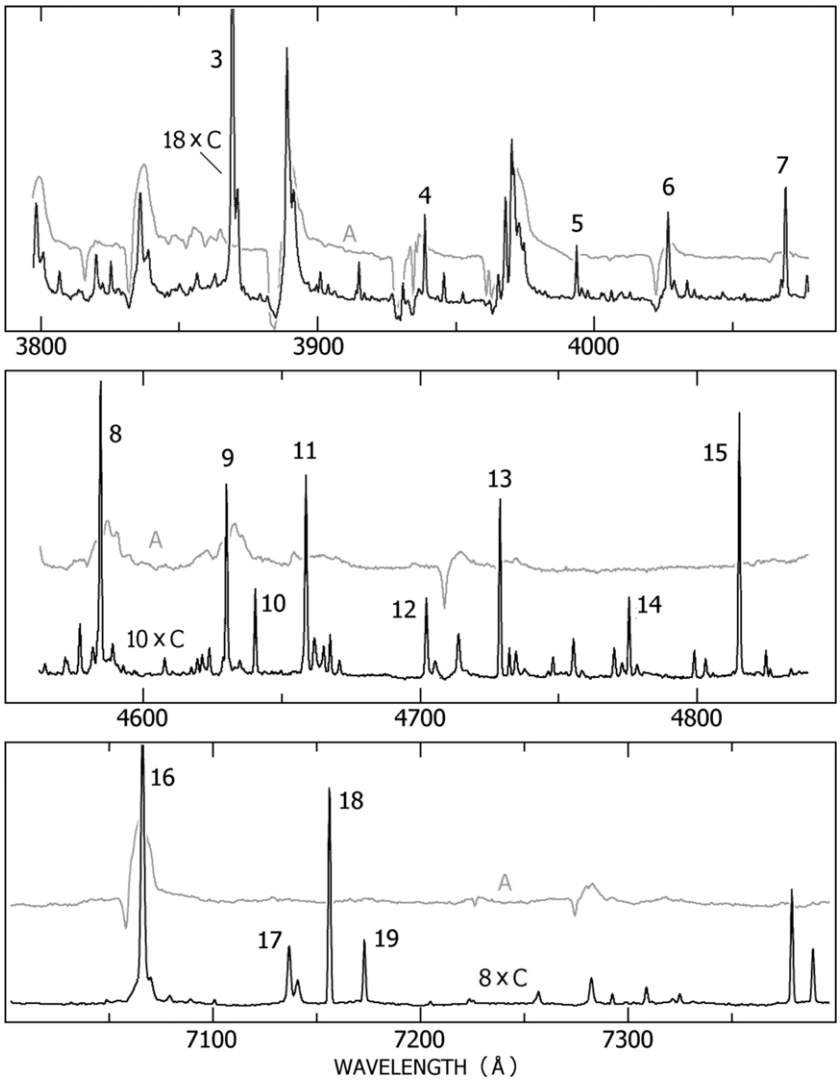

Figure 2. *HST*/STIS spectra showing the emission lines listed in Table 1. Gray tracings represent the central star, while black tracings show Knot C with magnified flux scales. The bottom of each panel corresponds to zero flux. Within each panel, the linear vertical scale is approximately the same for both tracings with a spectrum extraction width of about 100 mas.

the spatial sampling can be improved by "dithering," i.e., by taking separate observations at positions that differ by (integer + 0.5) pixels along the spectrograph slit. Our data were obtained in this way, as listed in Table 2. Two nominal slit positions were used, with the same midline and differing in the observing plan by $\Delta x \approx 228$ mas ≈ 4.5 pixels along the slit. The 4.5 pixel difference, rather than 0.5, ensures that each x-locale is sampled by two different sets of physical pixels. We measured the true offsets Δx as explained below. The available observing time allowed only enough wavelength coverage to include the best moderate and high excitation features plus [Fe II] λλ2508, 2509 (Mehner et al. 2010; Hamann 2012).

Instead of the "drizzling" process usually applied to dithered *HST* images, we used a careful procedure described below. Since it requires the original, geometrically unaltered CCD rows and columns, we worked with "semi-raw" data: flat-fielded, with cosmic-ray hits and average underlying count levels removed, but omitting wavelength calibration and corrections for optical distortion. Cosmic-ray removal was based on multiple exposures at each dither location ("CR-SPLIT," N in Table 2). We considered treating each individual exposure separately and allowing for cosmic-ray hits at a later stage in the process, but concluded that this would give little advantage in practice. In fact, the final results were consistent enough to be self-verifying.

A few definitions are needed. Let u and x denote CCD column and row number, respectively, not necessarily integers because they may refer to an interpolated position. To a first approximation, u represents wavelength while x represents spatial position along the slit (Figure 1). If $F(u,x)$ denotes intensity incident on the detector, then of course the CCD records only $f(u_m, x_n)$, the average of F in each physical CCD pixel. Regarding $f(u,x)$ as a continuous function, we estimated values between data points by cubic spline interpolation. For the measurements in Sections 3.2–3.4, we used a complete dither pair for each interpolation, so the x-interval between data points was approximately 0.5 pixels rather than 1 pixel.[8]

Deriving $F(u,x)$ from $f(u,x)$ is a non-trivial task, but fortunately the main results are apparent from the unenhanced

[8] Along any column in a single STIS spectrogram, spline interpolation gives erratic results because of the inadequate sampling (Davidson 2006). Interpolation within a properly dithered data set is far more satisfactory. Strictly speaking, our interpolation procedure included additional sub-steps that turned out to be unnecessary. We omit them here because they had no practical effect and explanations would be very lengthy.

Table 2
Dithered *HST*/STIS/CCD Observations[a]

Root Number[b]	Wavelength Range (Å)	Position[c] (pixels)	Δt[d] (s)	N[e]
ob6064150	2480–2680	510.129	200	2
ob6064160	”	514.641	200	2
ob60640s0	3795–4075	514.995	6	2
ob60640u0	”	519.488	6	2
ob60640t0	”	515.031	54	3
ob60640v0	”	519.534	54	3
ob60640j0	4565–4845	513.161	10	2
ob60640l0	”	517.648	10	2
ob60640k0	”	513.183	60	4
ob60640m0	”	517.681	60	4
ob60641b0	7000–7565	517.615	21	3
ob60641d0	”	522.122	21	3

Notes.
[a] Obs. 2010 March 3, MJD 55258.7 = J2010.17, and *HST* Program GO 11612 (PI: K. Davidson).
[b] ID label in the *HST* archive.
[c] “Position” means the measured CCD row number of the central star continuum (x_A in Figure 1 and Section 3.1) at column 494 near the middle of the CCD. See the text for slit parameters, etc.
[d] Integration time (= total exposure time).
[e] N = CR-SPLIT, the number of separate exposures combined to make an “observation.”

f-profiles. Our procedure did *not* include deconvolution, mainly because no trustworthy PSF was available and also because such a process may amplify the effects of pixel noise and other high-spatial-frequency defects. At any rate, it proved to be unnecessary (Sections 3.4 and 4.4).

3.1. Measuring the Spectral Trace

Spatial position is not exactly constant along a given CCD row; a spectrum “trace”—the locus of a point-source continuum across a spectrogram—is slightly tilted and curved. Typically an STIS trace may shift by 1 row in about 150 columns ($dx/du \sim 0.007$), but this slope varies considerably among the various gratings and grating tilts. Routine spectrum extractions take these facts into account, of course; but our problem requires unusual spatial accuracy. We measured the central star’s trace $x_A(u)$ in each spectrogram to high precision by the following method.

Consider an observed column vector $f(x)$ at a given u in one exposure, interpolated so that it is a continuous function. It may be the average of several adjacent columns, avoiding emission features. Local interpolation errors due to inadequate spatial sampling have very little effect when the following procedure is completed. The centroid of $f(x)$ is close to the star’s position, but is mildly perturbed by the Weigelt knots, by noise, and especially by asymmetry of the PSF. A precise and consistent position measure can be obtained as follows. First adopt a local weighting function $\phi(s) = 1 - (s/a)^2$ for $|s| < a$ and 0 elsewhere, with $a = 4$ pixels ≈ 203 mas. At any given position x along the column, define a local quantity:

$$X(x) \;=\; \frac{\int x' f(x')\,\phi(x'-x)\,dx'}{\int f(x')\,\phi(x'-x)\,dx'}. \qquad (1)$$

Thus $X > x$ or $X < x$, respectively, on each side of the major peak of $f(x)$ due to the star. A robust modified-centroid location x_A is then defined by

$$X(x_A) \;=\; x_A. \qquad (2)$$

Function $\phi(s)$ suppresses pixels that add noise but little information, and it also reduces pixelization effects.

For any given CCD column u, we search for the position x_A that exactly satisfies Equation (2), and we adopt it as the position of the star in that column. If an asymmetric PSF causes x_A to differ from the true position by a small amount, then other spatial features will have the same offset so their *relative* positions $x - x_A$ are meaningful to high accuracy. We determine the trace $x_A(u)$ by fitting a cubic polynomial to the values measured in a set of well-spaced columns. A detailed analysis of this method would be too long for this paper, but the main advantages are: (1) it is conceptually simple, (2) the iterative procedure is easy to implement, (3) it averages over pixel noise about as well as any method can, (4) results are consistent without any need to know the parameters of the asymmetric STIS PSF, and (5) if enough sample columns are used, the resulting $x_A(u)$ is quite insensitive to the STIS sampling problems described in Davidson (2006). This last fact is true because the slope of the trace dx_A/du amounts to “virtual dithering” so far as the cubic fit is concerned. In other words, x_A coincides with a CCD row in some columns, it falls halfway between row midlines in some other columns, etc., and altogether these average out in the cubic fit.

In each spectrogram listed in Table 2, we chose 10 well-spaced column locations u, corresponding to wavelengths that avoided perceptible emission and absorption lines. For each of these samples, the adopted $f(x)$ was the average of five adjoining CCD columns centered at u. Then we used the 10 sample values $x_A(u)$ to compute the least-squares cubic fit for $x_A(u)$ in that spectrogram. Based only on counting statistics, the formal error of each fit was less than 0.01 pixels or 0.5 mas across most of the observed range of u. (This statement is based on Monte Carlo simulations.) Systematic effects, e.g., due to the asymmetry of the STIS PSF, can be larger but have almost no effect on the relative differences $x - x_A$ which ultimately determine our results.

Corresponding dither pairs (Table 2) provide an obvious consistency test. Ideally their traces $x_A(u)$ should differ by a constant $\Delta x = 4.5$ pixels, the offset specified in the observing plan. In fact, the rms value of $(\Delta x - 4.5)$ for the six dither pairs in Table 2 is 0.009 pixels ≈ 0.5 mas. Variations across the CCD are larger because of image distortions in the STIS. An example: evaluating the cubic-fit dither offsets Δx at wavelengths of relevant emission lines in the short-exposure 4565–4845 Å dither pair, we find $4.484 \lesssim \Delta x \lesssim 4.510$; a range of 0.026 pixels ≈ 1.3 mas. Altogether, the estimated star position $x_A(u)$ appears to be consistent within $\pm$ 1 mas at most wavelengths, only 2% of the instrumental resolution. Of course, this high quality required a large number of data pixels for each fit. The instrumental variations of spatial scale are negligible for our purposes, partly because we employ only a few of the CCD rows running through the central part of the detector. The main point is that errors in the trace $x_A(u)$ are much smaller than the effects of interest which exceed 10 mas (Section 4). Some extra tests not worth detailing here were also applied, such as comparisons between independent dither pairs. They all had satisfactory outcomes.

Therefore, when examining the spatial position of an emission line in the Weigelt knot C, we can safely refer to a true spatial coordinate

$$z \;=\; x - x_A(u), \qquad (3)$$

where $x_A(u)$ is known to high accuracy.

3.2. Subpixel Modeling

As noted earlier, dithering along the slit is essential because the STIS/CCD spatial sampling is too sparse to take full advantage of *HST*'s basic resolution.[9] For any given CCD column u, a dither pair of spectrograms provides two sample vectors:

$$f_n^{(1)} = f(n) \text{ and } f_n^{(2)} = f(n + \Delta x - 4), \quad (4)$$

where the dither offset Δx is a known function of u based on the measured traces $x_A(u)$. The two vectors together provide a sampling interval of about 0.5 CCD pixels or 25 mas, nearly adequate for *HST*'s resolution according to the Nyquist criterion. For each relevant column or sum of adjoining columns, we used cubic spline interpolation to derive a continuous function $f(x)$. (Of course, this interpolation employed the true Δx values, not the uniform nominal spacing of 0.50 pixel.) Then we shifted each $f(x)$ to produce $f(z)$, a spatial distribution relative to the star's position (Equation (3)).

We half-expected the two parts of each dither pair to differ perceptibly in their intensities and PSFs—due, e.g., to variations of the "jitter" in the *HST* pointing, slight drifts perpendicular to the slit, electronic subtleties, etc. In fact no such differences were found.

3.3. Removal of the Central Object

As noted in Section 2 and Figure 1, we must subtract a "continuum" spatial profile $f_1(z)$ from the spatial distribution $f_2(z)$ measured at each narrow emission line. The underlying f_1 represents mainly the central star but also includes continuum and dust-reflected light from knot C. In order to estimate the relevant f_1 values, we sampled spatial profiles at various wavelengths that had no perceptible emission features. In order to avoid biased sampling in the x-direction, we included pairs of wavelengths whose trace positions $x_A(u)$ differed by substantially non-integer numbers of pixels (Section 3.1).

Within each observed wavelength interval, $f_1(z)$ varied with wavelength less than one might expect. The optical diffraction limit by itself would imply a narrower spatial PSF near the short-wavelength end of an interval. But this is counteracted by poor STIS focusing on the shorter-wavelength side of the CCD; see Davidson (2006) and the instrument handbook.[10] For instance, we found widths between 1.524 and 1.561 pixels (FWHM) for $f_1(z)$ across the interval 4585–4810 Å—a range of only 2.4% even though the wavelength varied by 5%.

In each panel of Figure 3, the lower trace $f_1(z)$ depicts the envelope of four separate profiles in that wavelength range. Larger variations were found in the other three wavelength ranges, but for each emission line we used nearby samples of $f_1(z)$. In the important case of [Ne III] λ3870, for example, we found an FWHM between 1.663 and 1.669 pixels across the interval 3850–3950 Å. These f_1 widths represent combinations of the basic instrumental PSF, imperfect optical focus, *HST* jitter, and very likely a real non-point-like width of η Car's wind; for our purposes, there is fortunately no need to know the relative size of each effect. The star's spectrum is more complex at UV wavelengths 2480–2680 Å, but the strange Fe II λλ2708, 2709

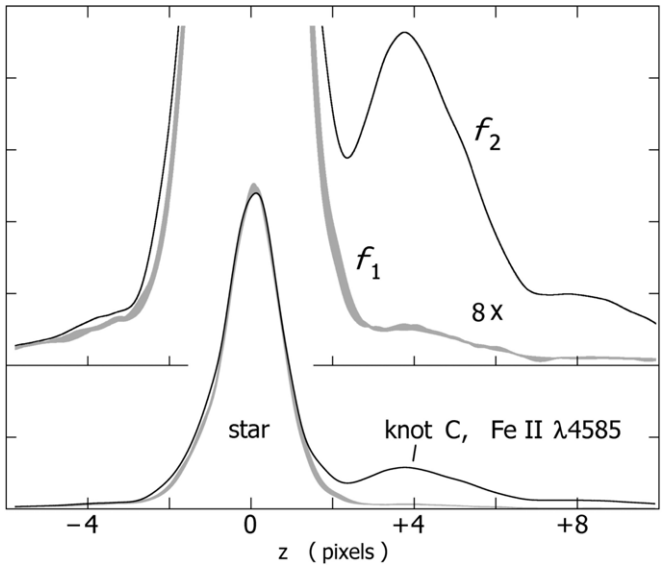

Figure 3. Observed spatial profiles along the slit near λ ∼ 4585 Å. The two panels differ only in their vertical scales. In each panel, the upper trace f_2 represents a wavelength at the center of the Fe II λ4585 emission line. The lower trace f_1 shows the *envelope* of four independent samples at wavelengths with no perceptible emission features. The five samples were renormalized, so they approximately match in the brightest part of the star image.

lines are extremely bright in the Weigelt knots, easy to separate from the star.

Subtracting $f_1(z)$ from each narrow-emission-line profile $f_2(z)$ therefore presented no serious difficulty. This is manifestly true for the brightest measured lines, which considerably exceeded the underlying $f_1(z)$. Figure 3 shows one such case, Fe II λ4585 (see Table 1). For each narrow emission line, we simply used the measured profile f_1 that was closest in wavelength. In each case f_1 was renormalized to match the integrated brightness of f_2 at the star's peak. (Strictly speaking, we based the adjustment factor on the maximum values of $q(z) = \int \psi(z - z')f(z')dz'$ for f_1 and f_2, where ψ is a parabolic weighting function only 1 pixel wide. Other definitions give practically the same results.) This renormalization is not exactly valid if the narrow emission line extends across the star image; but any resulting error in the difference $f_2 - f_1$ is very small at the location of knot C, because $f_1(z_C) \ll f_1(0)$; see Figure 3. In recent years, the narrow emission lines along our line of sight to the star have been quite faint compared to the star itself (Mehner et al. 2010).

Figures 4 and 5 show examples of net profiles $g(z) = f_2(z) - f_1(z)$. Numerical oscillations occur at the location of the star, $-2.3 \lesssim z \lesssim +2.3$, because the net values there are differences between two very large quantities which are nearly equal but slightly imperfect. As one expects from Figure 3, the Weigelt knot is represented quite well for $z \gtrsim 2.5$ pixels—much better than in any non-spectroscopic *HST* image. Separate dither pairs (independent sets of STIS exposures) gave $g(z)$ profiles that mutually agreed to within the uncertainties set by counting noise. He I profiles tend to be less satisfying than the others, for a reason noted in Section 4.

Incidentally, Figure 3 illustrates the difficulty of measuring a Weigelt knot in standard images. In continuum light, knot C appears only as a small bump in the f_1 tracing near $z \sim 4$ pixels, scarcely brighter than the star's PSF at that location. By contrast, the narrow emission line greatly exceeds the star in that locale; compare curve f_2 to f_1 in the figure.

[9] This statement is not equivalent to the distinction between $f(x)$ and $F(x)$ mentioned earlier, though it is related. See Davidson (2006).
[10] http://www.stsci.edu/hst/stis/documents/.

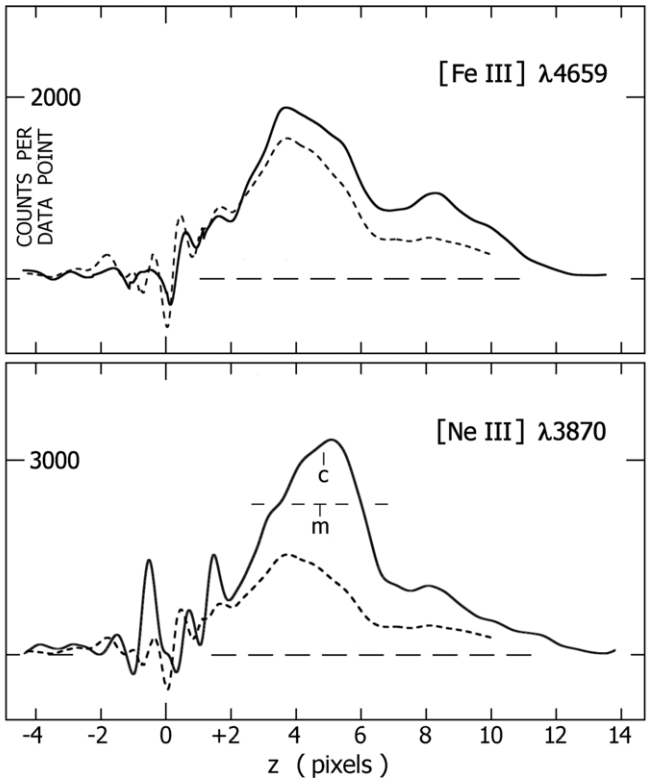

Figure 4. Net spatial profiles $g(z)$ for the [Fe III] λ4659 and [Ne III] λ3870 emission lines in knot C. For the latter, points "m" and "c" are "midpoint" and "centroid" positions defined in Section 3.4. Dashed curves show the average spatial profile of four [Fe II] lines; see the text in Section 4.

3.4. Measuring the Positions

The most reliable part of the net spatial profile $g(z) = f_2(z) - f_1(z)$ is obviously near its peak; see Figures 3 and 4. Therefore, we based our position measurements on the 70%-of-peak level. For each narrow emission line the procedure was as follows. Begin with the available dithered data points along the appropriate CCD column, i.e., at half-pixel intervals of z. Via cubic splines, these define a continuous spatial profile $g(z)$. Denote by z_a and z_b the two places where $g(z) = 0.7\,g(\text{peak})$. Then, if $h(z)$ is the quantity $g(z) - 0.7\,g(\text{peak})$, one can easily calculate a "midpoint" and a "centroid":

$$z_m = \frac{z_a + z_b}{2} \quad \text{and} \quad z_c = \frac{\int z\,h(z)\,dz}{\int h(z)\,dz}\,, \tag{5}$$

with integration limits z_a and z_b. The difference $z_c - z_m$ indicates asymmetry near the line peak. Examples are shown in the lower panel of Figure 4. In most cases, we use the simple average $\hat{z} = 0.5\,(z_m + z_c)$.

We estimated statistical uncertainties by performing random simulations with profiles like those shown in Figure 4. Several types of statistical errors occur. (1) Most important is the counting noise associated with the square root of $f_1 + f_2$. For a net profile g with a peak of 1500 counts per data point, the resulting rms error in either z_m or z_c was found to be roughly ±0.07 pixel. Noise errors are of course worse for fainter profiles. (2) Imperfect spatial sampling also has an effect, because the precise cubic-spline fit $g(z)$ depends on the location of the pixel array relative to the spatial profile. This depends on the profile shape, but we estimated typical rms errors in the range ±0.003 to ±0.01 pixel. These do not depend on the strength of the emission line. (3) According to Section 3.1, errors in the spectral trace $x_A(u)$ are not worse than ±0.03 pixel. Uncertainties quoted above are formal statistical estimates, and *systematic* errors may be larger (Section 4.1).

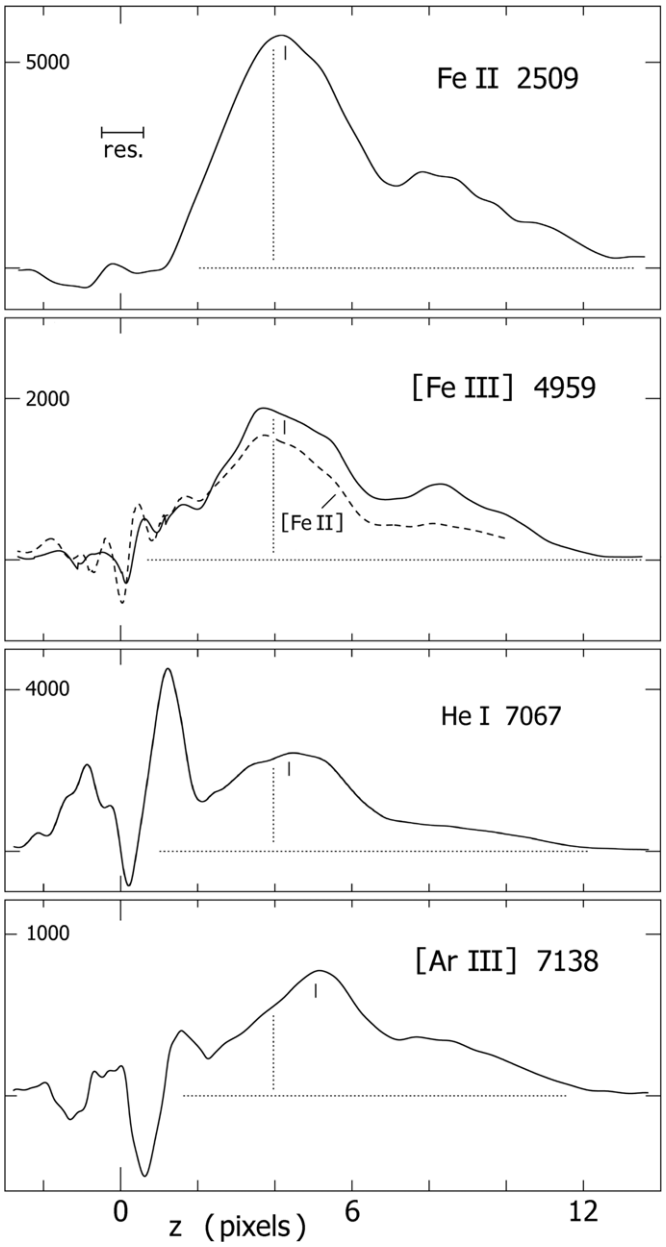

Figure 5. Spatial profiles $g(z)$ for several emission features with differing characteristics. A small vertical mark shows $\hat{z}$ for each feature, defined in Section 3.4. The dashed curve is the average of four [Fe II] lines, the same as in Figure 4. The vertical dashed line shows their average $\hat{z}$.

In principle, one-dimensional Lucy–Richardson deconvolution can enhance the spatial resolution; but a few trial examples showed no worthwhile improvement with these data. Knot C appears to be partially resolved without deconvolution, having FWHM ∼ 3.6 pixels ∼ 180 mas (Figure 4)—i.e., almost three times as wide as the overall PSF. Since deconvolution tends to magnify small numerical irregularities and noise at high spatial frequencies, we chose not to employ it.

4. RESULTS

Figures 4 and 5 show some of the measured spatial profiles $g(z)$. As a reference for comparison, in each figure a dashed

Table 3
Measured Positions

Feature and Category[a]			u[b]	Peak[c]	z_c[d]	z_m[d]	err[e]
1	Fe II λ2508	X	183	4350	4.426	4.394	±.06:
2	Fe II λ2509	X	193	5660	4.256	4.290	±.06:
3	[Ne III] λ3870	H	269	3320	4.844	4.740	±.055
4	Fe II λ3939	L	519	890	3.939	3.990	±.100
5	[Ni II] λ3994	L	717	670	4.270	4.269	±.120
6	He I λ4027	H	836	730	4.258	4.332	±.120
7	[S II] λ4070	L	990	1310	4.138	4.216	±.085
8	Fe II λ4585	L	91	2570	3.869	3.946	±.060
9	Fe II λ4631	L	255	1830	3.698	3.671	±.070
10	[Fe II] λ4641	L	293	890	4.073	4.130	±.100
11	[Fe III] λ4659	M	359	1880	4.182	4.310	±.070
12	[Fe III] λ4703	M	516	770	4.384	4.325	±.110
13	[Fe II] λ4729	L	612	1860	3.895	3.997	±.070
14	[Fe II] λ4776	L	781	850	3.766	3.721	±.110
15	[Fe II] λ4816	L	926	2640	3.990	4.026	±.060
16	He I λ7067	H	127	2430	4.396	4.332	±.060
17	[Ar III] λ7138	H	254	780	5.102	5.023	±.110
18	[Fe II] λ7157	L	289	3330	4.152	4.161	±.055
19	[Fe II] λ7174	L	319	970	4.084	4.091	±.100

Notes.
[a] See Table 1.
[b] Approximate STIS/CCD column (1–1024), cf. Table 2.
[c] Approximate maximum net counts per data point in knot C.
[d] Centroid and midpoint distances from the star, expressed in CCD pixels (∼50.7 mas).
[e] Estimated rms statistical errors in z, not including systematic effects that may be larger.

Table 4
Measured Distances from the Star

Ionization Category[a]	$n_{\rm lines}$[a]	Median $\hat{z}$ (mas)[b]	Range of Values (mas)
L	11	204	187–217
M	2	218	216–221
H	4	232	218–257
H'[c]	2	249	243–257
X	2	220	216–224
I1[d]	(dust?)	(229)	...
I2[e]	(dust?)	(237)	...

[a] See Table 1.
[b] Projected distance from star, assuming CCD pixel width = 50.71 mas.
[c] Omitting He I for reasons noted in Section 4.
[d] I1: the location of knot C′ in Chesneau's 2002–2005 near-IR image data, corrected for expansion to 2010. See Figure 4 in Artigau et al. (2011).
[e] I2: location in 2010 "predicted" from *HST* image data, probably less accurate than I1. See Figure 11 in Smith et al. (2004).

curve shows the unweighted average of four [Fe II] features labeled 10, 13, 14, and 15 in Tables 1 and 3.

The most surprising result concerns spatial location z as a function of ionization level, shown in Tables 3 and 4 and Figure 6. *Highly excited features obviously tend to occur farther from the star, i.e., at larger z, not closer to the star as was expected* (Section 1). Two very different statistical analyses in Sections 4.1 and 4.2 confirm the reality of this effect. Before reviewing likely errors, it is important to recall that our measurement procedure was blind to ionization and excitation level; the various emission lines occurred at essentially random columns on the detector, and they were all treated alike. Note also that [Ne III] and [Ar III], the conspicuously highest points in

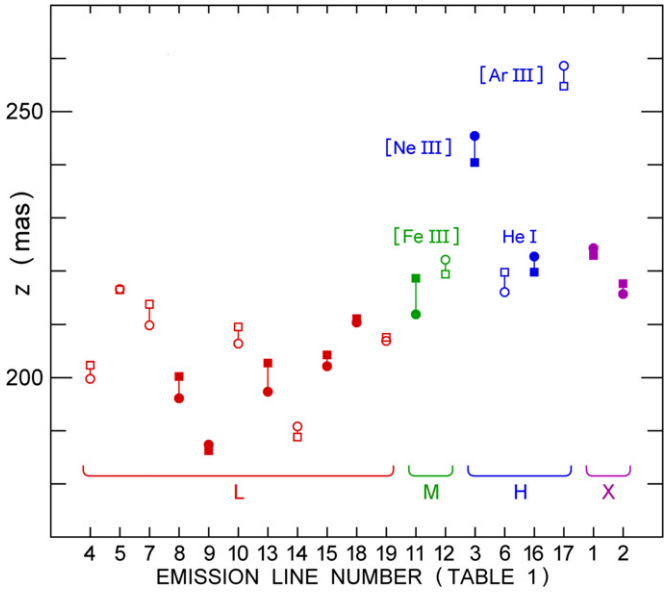

Figure 6. Position measurements of emission lines relative to the star, sorted by ionization category. These are the results listed in Table 3; filled symbols represent features with higher count rates. Circles and squares indicate z_c and z_m, respectively; see the text.

Figure 6, probably represent ionization category H better than the He I lines do. [Ne III] and [Ar III] originate mainly in the highest-temperature gas, while the He I recombination lines are less sensitive to temperature and tend to favor the coolest parts of the He^+ zones (Osterbrock & Ferland 2006; Davidson & Netzer 1979). Moreover, η Car's stellar wind produces substantial He I features, which may perturb our He I positional measurements toward slightly smaller values of $\hat{z}$; indeed this is obvious for He I λ7067 in Figure 5. Therefore, Table 4 summarizes the $\hat{z}$ values for two versions of category H: with and without the He I lines.

4.1. Statistical Significance Based on Measurement Quality

One form of confidence level involves the measurement uncertainty. We can estimate this quantity based on the scatter of either z_m or z_c among the nine Fe II and [Fe II] features listed in Table 1. In principle, the forbidden lines might differ from permitted lines because the latter have higher upper energy levels; but in fact we find no statistically significant difference between the six [Fe II] lines and the three Fe II features. If all of them have the same true average position, then the scatter in measured values indicates an rms error of about ±0.17 pixel or ±8.6 mas for both z_m and z_c. This is roughly twice as large as the semi-formal statistical uncertainty estimated in Section 3.4. Therefore, undiagnosed effects of the order of ±7 mas—instrumental subtleties and/or imperfect assumptions about the emission—probably dominate the error budget. This is a common, or even usual, circumstance for sensitive astronomical measurements.[11] Such effects can probably be treated like random errors here, because, as noted above, the wavelengths, detector locations, and intensities were not seriously correlated with emission-line category or excitation. If all the $\hat{z}$ values are systematically too high or too low, this has no effect on differences between emission categories.

[11] Real positional differences may exist among the Fe II and [Fe II], but theoretically there should be almost no difference between lines 10 and 13 (multiplet 4F) or between lines 14 and 15 (multiplet 20F).

Now consider the unweighted average of $\hat{z}$ for each ionization category. If the rms error for an individual line is ±8.6 mas as suggested above, then the formal averages are 203 ± 2.5 mas for ionization category L ($N = 11$ spectral features) and 229 ± 3.5 mas for categories M and H together ($N = 6$), a 6σ difference. If, pessimistically but somewhat illogically, we base the individual measurement uncertainty on the larger scatter within data set M ∪ H, then the difference is still 3.4σ. If we omit the weakest lines in each category, or if we omit the intermediate category M, then the confidence level becomes stronger. In summary, the conclusion that $\hat{z}(\mathrm{M} \cup \mathrm{H}) > \hat{z}(\mathrm{L})$ is well established so far as random errors are concerned.

The relatively large scatter in $\hat{z}$ within categories M and H is not surprising. [Fe III] represents a lower-ionization zone than [Ne III], [Ar III], and He I, while all these lines span a range of temperature dependences.

4.2. A Different Approach to Statistical Significance

If one is skeptical about the rms measurement errors reported above, another form of reasoning does not require them. Consider, for example, the following statement about the strongest emission lines, the filled symbols in Figure 6. *All three of the $\hat{z}$ values in ionization categories M and H exceed all five of those in category L.* If they were all random samples of one population, the probability of this outcome would be less than 0.02. This type of test is valid for any reasonable population distribution. The fainter lines strengthen the case. Suppose that the 11 measurements in category L and the six in categories M and H constitute two sets of random samples. (Differences in quality may alter this assumption, but more elaborate analyses lead to the same conclusion.) *All of the $\hat{z}$ values in set* M ∪ H *are higher than the second-largest value in set* L. If both sets were drawn from one population, the probability of this outcome would be less than 0.0006. If we further note that only one value in set M ∪ H lies below the highest in set L, this becomes a problem in multinomial coefficients (e.g., DeGroot & Schervish 2002) and the probability falls below 0.0002. Set M ∪ H thus differs from set L with a high confidence level, whether we use all the spectral features or only the best ones. This statement does not require any knowledge of the measurement errors.

4.3. Concerning Systematic Errors

Although the measurement procedure was blind to ionization state as noted above, there is an obvious danger in the small number of suitable high-ionization features. Subtle effects involving location on the CCD detector might conceivably influence the results merely because the distribution of [Ne III], [Ar III], and [Fe III] lines was sparse. Fortunately, we can assess this possibility via the low-ionization lines. In the best grating-tilt wavelength interval, 4565–4845 Å (Table 2), three category L lines have smaller wavelengths than [Fe III] and three have larger wavelengths; together they show no trend large enough to affect the result for [Fe III]. The 3795–4075 Å interval is less satisfactory because all three measurable category L lines there have longer wavelengths than [Ne III] λ3870—but the $\hat{z}$ value for that feature is so large that a hypothetical wavelength-dependent effect would need to be far greater than any comparison lines suggest. A similar remark applies to [Ar III]. In summary, the low-ionization features appear to confirm what one expects from the nature of the instrument, i.e., that there is no serious wavelength-dependent error in our measurement procedure within each spectrogram.[12]

4.4. Other Potentially Important Findings

Weigelt knot C is partially resolved in the light of emission lines, with an FWHM ∼ 180 mas for a typical line compared to about 80 mas for the star image (Figures 3–5). Therefore the true, deconvolved FWHM is probably between 150 and 170 mas, or about 370 AU at η Car's distance. Near-IR data give the same extent for dust in the knot; see Figure 4 in Artigau et al. (2011). Ionization categories L, M, H, and X spatially overlap each other to a great extent. This is not surprising, since we view the ionization structure from an oblique angle relative to the star–knot radial vector. Note, however, that the spatial profiles for [Ne III] and [Ar III] are both strongly skewed toward larger z. This fact by itself is enough to distinguish those two highest-ionization features from most of the others. On average, the low-excitation emission appears skewed in the opposite direction. We have not attempted to model the asymmetric spatial profiles shown in Figures 4 and 5.

Those figures also show a second obvious brightness peak around $z \approx 8.4$ pixels ≈ 430 mas. Based on this and previous hints (e.g., Section 3.2 in Mehner et al. 2010), evidently the emission morphology has numerous local spots, not just the three classic Weigelt knots. The example shown in our data must be roughly aligned with the star and knot C. Faint material can be perceived near that location in some *HST* images (Smith et al. 2004), but it seems uncertain there for the reasons noted in Section 2. In any case, the STIS results define this outer knot fairly well, and they show that it is almost half as bright as knot C in emission-line categories M, H, and X (Figures 4 and 5). Since the outer knot does not show a clear peak in the lower ionization features, we did not attempt to detect ionization structure there. The most effective way to map the region is to use STIS spectra with a set of slit positions and with spatial dithering parallel to the slit—a task that no one has attempted.

Small Doppler velocity effects may accompany the positional differences shown in Figure 6. Routine wavelength measurements show no significant velocity trends among the categories of emission lines, but the differences may be too small to detect without a special effort. The individual lines' velocity profiles probably differ as well. A velocity investigation with unusually precise wavelength calibrations, etc., is beyond the scope of this paper, because it would require as much additional effort as the steps reported above. Zethson (2001) and Zethson et al. (2012) list many emission velocities in the Weigelt knots with ordinary accuracy, including all the features in Table 1.

Figure 6 shows that the mysterious Fe II λλ2508, 2509 emission arises at about the same location as [Fe III], farther from the star than the low-excitation features. We cannot explore the applicable models here, but this result should help to constrain them (see Johansson & Letokhov 2004; Hamann 2012, and references therein).

5. DISCUSSION

The unexpectedly inverted excitation structure—with higher-ionization species relatively farther from the star rather than closer—is not easy to explain. Very likely it is a clue to

[12] Optical distortions are negligible in the narrow range of CCD rows used here; see the instrument handbook at www.stsci.edu/hst/stis/documents/. In order to nullify the [Ne III] result, one would need a spatial-scale variation of the order of 10% between 3870 Å and 4000 Å.

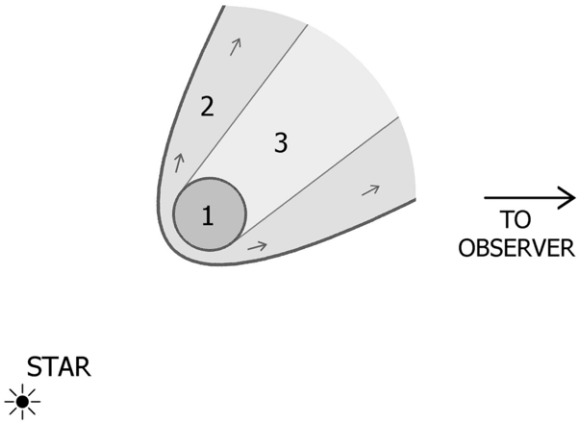

Figure 7. "Ablation" caused by photoionization. Zone 1 is a dense low-ionization cloud, zone 2 contains outward-flowing gas photoionized by the star, and zone 3 is shadowed. Emission lines from zone 2 might on average originate higher than zone 1 in this diagram; see the text. This is merely a qualitative sketch of one possibility.

some previously unrecognized aspect of the Weigelt knots' morphology.

The most obvious idea, excitation by an outer bow shock, fails for at least two reasons. First, this conjecture would require ambient gas moving either *slower* than knot C relative to the star or else inward. Since the knots' velocities are themselves very slow in the context of η Car, and the vicinity should have been swept out by two eruptions and the stellar wind, this seems very unlikely. There is no emission-line evidence for motionless or inward-moving gas. A second objection concerns the energy budget. The mass of visible, unobscured material in Weigelt knots B, C, and D is of the order of 0.01 $M_{\odot}$ (Hamann 2012; Davidson et al. 1995), implying kinetic energy $\sim 10^{44}$ erg at the observed speed of roughly 40 km s^{-1}. Even if this is converted into emission lines within only 100 yr, the total luminosity of all the lines would be less than $10^{34.6}$ erg s^{-1}, several orders of magnitude too small. Moreover, this is an optimistic estimate since the knots do not appear to be decelerating that rapidly, and because most of the energy of a shock dissipates through expansion rather than line emission. The bow shock idea therefore appears highly implausible.

Lesser shocks or other material waves moving through the knots are similarly unappealing. In order to excite even a fraction of the observed emission, they would need to carry so much energy and momentum that the knots would be disrupted within a few years. UV photons from the star, on the other hand, can heat and excite the knots because they carry far less momentum per unit energy.

Most likely, some relatively low-density high-ionization zones exist around knot C, with a geometry that somehow allows most of the photoionizing energy to be reprocessed in regions slightly farther from the star than is the center of the knot. It would be useful to have spatial measurements along a slit perpendicular to the orientation that we used, but unfortunately no such data exist.

Figure 7 shows one possibility. When a gas condensation is illuminated by ionizing photons, heated material can "evaporate" through an expansion front. In favorable circumstances, the escaping gas flows outward around the condensation, accelerated by radiative forces exerted via photoionization: zone 2 in the figure. One might call this process photo-ablation or photo-evaporation, and it can produce a rocket effect that we are not concerned with here. Because zone 2 is less dense and is directly exposed to the central star, it should produce mainly high-ionization category-H emission lines. As Figure 7 illustrates, emission lines from zone 2 may appear preferentially on the *outer* side of the condensation itself (zone 1), in our projected view.

Admittedly the densest emission region should be near the expansion front, adjoining the inner edge of zone 1. The basic idea nevertheless remains viable, because those inward-facing regions may be partially obscured by dust in the condensation, and also for reasons involving the density-dependent [Ne III] and [Ar III] emissivities. A detailed model of the accelerated flow is needed in order to say whether the high-ionization lines should exhibit conspicuous velocity differences. If an explanation of this type is true, then it is potentially useful because the partially observable structure depends on parameters of the knot.

Conceivably a separate, unrelated *high-ionization* knot lies along a line of sight slightly farther from the star than the center of knot C, thereby perturbing our [Ne III] and [Ar III] measurements. But this idea is somewhat artificial, because the hypothetical condensation must have a particular column density and scale size in order to produce enough localized high-ionization emission without comparable low-ionization features. A large, low-density cloud, for instance, could produce [Ne III], but its spatial gradients would be insufficient for the proposed effect. High-ionization knots have not been obvious in the large volume of existing STIS data near η Car. If the true explanation is in this vein, then it strongly suggests a widespread, highly inhomogeneous configuration of low-speed ejecta. One good test would be to examine Weigelt knot D; see a later comment below.

In an unconventional view, the Weigelt brightness peaks may represent minima in the intervening extinction, not physical condensations. We do not advocate this idea here, and we have not attempted to construct such a model, but it has not been ruled out and it would fundamentally alter the meanings of Figure 6 and Table 4. This question needs more comparisons between *HST* and IR maps (cf. Artigau et al. 2011). Precise Doppler velocities are worth investigating as noted in Section 4.4.

The spatial profiles in Figures 4 and 5 have other interesting implications. For example, the Weigelt knots originally appeared to be small condensations (Weigelt & Ebersberger 1986; Hofmann & Weigelt 1988), but in fact they have widths almost half as large as their distances from the star (Section 4.4 above, and Figure 4 in Artigau et al. 2011). This fact obviously affects theories of their origin and makes their proper motions more difficult to quantify (Section 2).

In Table 4, entries I1 and I2 are two estimates of $\hat{z}$ for dust in knot C, based on published measurements of non-spectroscopic images. Various emission lines also contribute, but the images were most likely dominated by hot-dust emission for I1 and dust reflection for I2. Chesneau et al. (2005) and Artigau et al. (2011), discussing the near-IR data used for position I1, carefully referred to knot C′, not C, to distinguish between the locations of dust emission and reflection. Thus, it makes sense that $\hat{z}$ for knot C′ (I1 in Table 4) is larger than the value for low-excitation emission lines. The I2 value, on the other hand, appears surprisingly large at 237 mas. It was based on *HST* images (Smith et al. 2004), and in a simple model it should have been in the neighborhood of 220 mas. We cannot explore this question here, but a likely guess is that irregularities in the PSF and other subtleties in the central star image led to systematic errors as hinted in Section 2. This issue matters because the

often-quoted Smith et al. (2004) analysis of the knots' proper motions and age relied on the same images and measurement techniques.

The other well-defined Weigelt knot, knot D, should be examined for ionization structure in the same way as knot C. Unfortunately, we have not been able to obtain *HST* observing time for suitably dithered observations. As a conceivable alternative approach, one might employ a large set of existing data. Many STIS observations of η Car in 1998–2011 used a slit position angle near 331° which samples knot D (see Mehner et al. 2010, and references therein). At a subpixel level, those data have more or less random placements of the star and knot along the slit—a form of accidental spatial dithering. However, since the star/knot brightness ratio has varied and we have no assurance that the knot's spatial profile has remained constant, a careful investigation along these lines would require more effort than the knot C analysis presented above.

In approximately the same manner as our ionization-zone analysis, *HST*/STIS data may be useful for two obvious additional tasks. First, this appears to be the best way to measure the Weigelt knots' proper motions and age at UV to red wavelengths. The main obstacle is a limited temporal baseline, beginning no earlier than 1998. Existing data near slit position angle 331° (see above) are pertinent in this connection. In principle, "virtual dithering" for each observation date might be obtained by using separate emission lines which peak at different fractional-row locations because of the slope of the spectral trace (Section 3.1).

A second interesting goal would be to map the region within 1″ of η Car in somewhat the same way as Mehner et al. (2010) but with higher spatial resolution. The fainter knot beyond C (Figures 4 and 5) is one example of why this would be useful; multiple brightness peaks in the region are very poorly known. This goal requires STIS observations that are spatially dithered along the slit, arguably more essential than dithering perpendicular to it. Unfortunately, no such data exist at present, except those used in this paper.

G.N.R. is supported by a Hertz Foundation Fellowship. We thank Beth Perriello and other consultants at STScI for assistance with the *HST* observing techniques.

REFERENCES

Artigau, É., Martin, J. C., Humphreys, R. M., et al. 2011, AJ, 141, 202
Chesneau, O., Min, M., Herbst, T., et al. 2005, A&A, 435, 1043
Davidson, K. 2006, in The 2005 HST Calibration Workshop, ed. A. M. Koekemoer, P. Goudfrooij, & L. L. Dressel (Baltimore, MD: STScI), 247
Davidson, K., Ebbets, D., Johansson, S., Morse, J. A., & Hamann, F. W. 1997, AJ, 113, 335
Davidson, K., Ebbets, D., Weigelt, G., et al. 1995, AJ, 109, 1784
Davidson, K., & Netzer, H. 1979, RvMP, 51, 715
DeGroot, M. H., & Schervish, M. J. 2002, Probability and Statistics, Section 1.9 (3rd ed.; Boston, MA: Addison-Wesley), 35
Dorland, B. N., Currie, D. G., & Hajian, A. R. 2004, AJ, 127, 1052
Hamann, F. 2012, in Eta Carinae and the Supernova Impostors, ed. K. Davidson & R. M. Humphreys (Astrophysics and Space Science Library, Vol. 384; New York: Springer), 95
Hofmann, K.-H., & Weigelt, G. 1988, A&A, 203, L21
Johansson, S., & Hamann, F. W. 1993, PhyS, T47, 157
Johansson, S., & Letokhov, V. S. 2004, A&A, 428, 497
Krist, J. E., Hook, R. N., & Stoehr, F. 2011, Proc. SPIE, 8127, 81270J
Mehner, A., Davidson, K., Ferland, G. J., & Humphreys, R. M. 2010, ApJ, 710, 729
Osterbrock, D. E., & Ferland, G. J. 2006, Astrophysics of Gaseous Nebulae and Active Galactic Nuclei (Sausalito, CA: University Science Books)
Smith, N. 2012, in Eta Carinae and the Supernova Impostors, ed. K. Davidson & R. M. Humphreys (Astrophysics and Space Science Library, Vol. 384; New York: Springer), 145
Smith, N., Morse, J. A., & Gull, T. R. 2004, ApJ, 605, 405
Verner, E., Bruhweiler, F., & Gull, T. 2005, ApJ, 624, 973
Weigelt, G., Albrecht, R., Barbieri, C., et al. 1995, Rev. Mex. Astron. Astrofis. Ser. Conf., 2, 11
Weigelt, G., & Ebersberger, J. 1986, A&A, 163, L5
Weigelt, G., & Kraus, S. 2012, in Eta Carinae and the Supernova Impostors, ed. K. Davidson & R. M. Humphreys (Astrophysics and Space Science Library, Vol. 384; New York: Springer), 129
Zethson, T. 2001, PhD thesis, Lunds Univ., Sweden
Zethson, T., Johansson, S., Hartman, H., & Gull, T. R. 2012, A&A, 540, A133